

Coalescence of Surfactant-Laden Droplets

Soheil Arbabi,¹ Piotr Deuar,¹ Mateusz Denys,¹ Rachid Bennacer,² Zhizhao Che,³ and Panagiotis E. Theodorakis*¹

¹*Institute of Physics, Polish Academy of Sciences, Al. Lotników 32/46, 02-668 Warsaw, Poland*

²*Université Paris-Saclay, ENS Paris-Saclay, CNRS, LMPS, 4 Av. des Sciences, 91190 Gif-sur-Yvette, France*

³*State Key Laboratory of Engines, Tianjin University, 300350 Tianjin, China*

(*Electronic mail: panos@ifpan.edu.pl)

(Dated: 26 June 2023)

Droplet coalescence is an important process in nature and various technologies (*e.g.* inkjet printing). Here, we unveil the surfactant mass-transport mechanism and report on several major differences in the coalescence of surfactant-laden droplets as compared to pure water droplets by means of molecular dynamics simulation of a coarse-grained model. Large scale changes to bridge growth dynamics are identified, such as the lack of multiple thermally excited precursors, attenuated collective excitations after contact, slowing down in the inertial regime due to aggregate-induced rigidity and reduced water flow, and a slowing down in the coalescence rate (deceleration) when surfactant concentration increases, while at the same time we also confirm the existence of an initial thermal, and a power-law, inertial, regime of the bridge growth dynamics in both the pure and the surfactant-laden droplets. Thus, we unveil the key mechanisms in one of the fundamental topological processes of liquid droplets containing surfactant, which is crucial in relevant technologies.

I. INTRODUCTION

Droplet coalescence plays an important role in many natural phenomena, for example, determining the size distribution of droplet rains^{1,2}, the dynamics of multiphase flows^{3,4}, and, also, in technological applications, such as inkjet printing⁵ or coating applications⁶. The coalescence process depends on the interplay between viscous and inertial forces and surface tension, with the minimization of the latter driving this process. Experiments, theories, and simulations of the coalescence of droplets without additives have provided great insight into its mechanisms^{7–25}, but much less is known in the case of surfactant-laden droplets^{4,26–43} or droplets with other additives^{44–51}, despite their relevance in many areas, such as cloud formation⁵², microfluidics⁵³, coating technologies⁵⁴, and water treatment during crude oil and natural gas separation⁵⁵. Based on high-speed imaging and particle image velocimetry technology, experimental studies have investigated the coalescence of surfactant-laden droplets, mainly providing macroscopic descriptions of the coalescence process^{35,36,38,56–58}. However, the initial fast stages of the coalescence process are impossible to observe in experiments due to device limitations.¹⁹ Moreover, conventional hydrodynamic models are only applicable in the later stages of coalescence^{59–61}, while the singularity at the initial contact point of the coalescing droplets continues to pose challenges for numerical modelling despite progress in this area^{11,13,23,56}. To address the latter issue, for example, continuum modeling may consider either the formation of a single body of fluid by an instant appearance of a liquid bridge that smoothly connects the two droplets and then evolves as a single body due to capillary forces, or a section of the free surface trapped between the bulk phases that gradually disappears¹³. In the case of systems with surfactant, continuum simulation has suggested that an uneven contraction of the interface due to a nonuniform distribution of accumulating surfactant at the meniscus bridge that connects the droplets is an important factor that modulates the surface tension, which, in turn, drives the coalescence process⁴. Still, numerical simulation is unable to analyze the mechanism of coalescence after the drops come into contact. Recent molecular-level simulations have clarified important aspects, such as the role of thermal capillary waves at the surface of water droplets¹⁰, but the effect of surfactant on the physics involved in the coalescence has remained overwhelmingly unexplored. We know surfactant effects must be large since they greatly change the surface tension, so the research reported here set out to clarify its role in the coalescence dynamics and other characteristics.

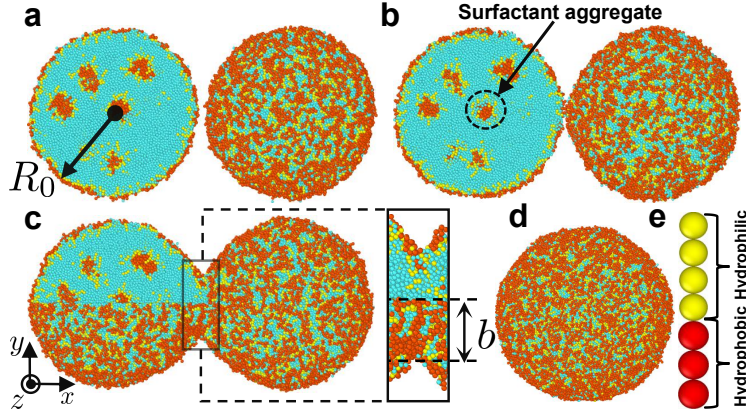


FIG. 1. Stages of coalescence of spherical surfactant-laden droplets with equal size and surfactant concentration (3.2 CAC). a) Initial configuration; b) Beginning of the bridge formation; c) Bridge growth with a magnified view of the bridge region. b is the radius of the bridge; d) Final equilibrium configuration after reshaping; e) Coarse-grained representation of a C10E4 surfactant molecule. The surfactant’s hydrophobic beads are in red, hydrophilic ones in yellow. Each cyan bead represents two water molecules. External or cross-section views are shown to highlight the bulk, surface, and bridge structure of the droplets. Surrounding water vapor is omitted for the sake of clarity. The snapshots of the system were obtained using Ovito software⁶⁷.

In this study, we report on large-scale MD simulations based on a high-fidelity coarse-grained (CG) force-field^{62–66}, which allows for the faithful simulation of surfactant in water. With these we uncover the mass transport mechanism of surfactant during coalescence, elucidate the dynamics of the bridge growth process, resolve the flow, and analyse how the above depend on surfactant distribution. We find an unexpected lack of multiple thermally excited precursor bridges, attenuated collective flow after contact, formation of new aggregates inside the bridge from surfactant previously at the droplets’ surface, and a slowing down in the inertial regime as surfactant concentration increases. In the following, we provide some background information in Sec. II. Then, we present our simulation model and methods in Sec. III and our results and relevant discussion in Sec. IV. Finally, we draw our conclusions and suggest possible directions for future work in Sec. V.

II. BACKGROUND

Droplet coalescence takes place in three different stages, namely, the droplet approach, when the two droplets are positioned close enough to ‘feel’ intermolecular forces (Fig. 1a), the bridge growth-stage (Figs 1b and 1c)⁶⁸, and the final reshaping stage towards the equilibrium spherical droplet (Fig. 1d). In the case of droplets without surfactant, the growth dynamics of the bridge has been investigated and in general, two different regimes have been assumed from the perspective of fluid dynamics^{11,56}: an initial viscous regime dominated by macroscopic flows that pull the droplets together, and a subsequent inertial regime, which involves the propagation of local deformations with higher Reynolds number excited near the bridge as it grows.

Even in the case without surfactant, the bridge growth dynamics has been under intense debate. In the viscous regime (VR), a linear scaling in time $b \propto t$ has been suggested for the bridge radius, b , as well as logarithmic corrections $t \ln t$ ^{11,56}, while a scaling $b \propto \sqrt{t}$ has been proposed for the inertial regime (IR)^{11,56}. However, others have suggested scaling regimes that depend on the ratio of characteristic scales to the viscous length scale, including an additional inertially limited viscous (ILV) regime,^{69,70} which, according to numerical simulations, is only realized when the coalescing drops are initially separated by a finite distance²¹. Another idea put forward has been the characterization of the viscous–inertia-regime transition via a modified Ohnesorge number in the case of immiscible droplets⁷¹. Despite the advent of modern experimental techniques, such as electrical measurements with resolution of a few micrometers⁷², the bridge growth dynamics at the early stages still remains challenging for experimental studies. Instead, molecular dynamics (MD) simulation of an all-atom model for water droplets has provided insight into this initial stage of coalescence, suggesting the formation of multiple precursor bridges at the pinch point, due to thermal capillary waves at the droplet surfaces¹⁰. These multiple bridges expand linearly in time, due to collective molecular jumps at the droplets’ interface, and the transition to the classical hydrodynamics regime only takes place when the bridge radius becomes larger than a thermal length, $l_T \approx (k_B T / \gamma)^{1/4} R^{1/2}$, assuming that fluctuations on one droplet are not affected by the other and in the absence of instabilities¹⁰. l_T describes the typical width of the contact points at droplet’s interface at the initial stage of coalescence, k_B is Boltzmann’s constant, T the temperature, γ the liquid–vapor (LV) surface tension, and R the radius of the droplet. Since l_T depends on surface tension, it is expected to grow with surfactant concentration as γ decreases,

saturating to a value, l_s , above the critical aggregation concentration (CAC) as γ reaches its plateau value.

In the presence of surfactant there are many unknowns. Several studies have suggested that its presence would actually delay the coalescence process, due to the reduction of the surface tension^{37,57}, while smaller droplets tend to show much faster equilibration of surfactant interfacial coverage^{38,73}. Moreover, it has been suggested that physical regimes could also depend on the diffusion and adsorption time scales of the surfactant, and their dependence on the surfactant concentration and the droplet size⁷³. In addition, it has been pointed out that surfactant alters the properties of the droplets particularly in the bridge area³⁹. For example, hydrodynamic instabilities, such as dimples, have been observed for concentrations larger than CAC⁴¹, but surfactant might actually have a more global effect by affecting the overall size of the droplets⁴⁰. Certain experiments have also highlighted the role of Marangoni flow that leads to local capillary pressure changes, which in turn affect the coalescence kinetics and result in a delay of the process^{4,36}. Despite these efforts, the mass transport mechanism of surfactants, the resulting dynamics and structure of the bridge and other early time effects are not well understood. Molecular simulations allow for tracking the individual molecules, which goes beyond the reach of any continuum simulation or real experiment and is therefore crucial for unravelling the mass transport mechanism of surfactant. At present, the early time phenomena that are pivotal for the onset of coalescence can only be investigated in adequate detail by molecular-scale simulation.

III. MODEL AND METHODOLOGY

Our investigation covers all stages of coalescence for droplets of equal size and surfactant concentration. We have considered different surfactants, such as C10E8 and C10E4⁶³, and a range of surfactant concentrations below/above CAC. The interactions between components of the system are obtained by the Mie- γ Statistical Associating Fluid Theory (SAFT Mie- γ)^{74–78}. The MD simulations were carried out in the canonical ensemble using LAMMPS software^{79,80}. After equilibration of each individual droplet, the droplets were placed next to each other for initiating their coalescence as illustrated in Fig. 1a.

The force field has been validated for water–surfactant systems with particular focus on accurately reproducing the most relevant properties of the system, such as surface tension and phase

behavior^{62–66,81–83}. Interactions between the various types of CG beads are described via the Mie potential, which is mathematically expressed as

$$U(r_{ij}) = C\varepsilon_{ij} \left[\left(\frac{\sigma_{ij}}{r_{ij}} \right)^{\lambda_{ij}^r} - \left(\frac{\sigma_{ij}}{r_{ij}} \right)^{\lambda_{ij}^a} \right], \text{ for } r_{ij} \leq r_c, \quad (1)$$

where

$$C = \left(\frac{\lambda_{ij}^r}{\lambda_{ij}^r - \lambda_{ij}^a} \right) \left(\frac{\lambda_{ij}^r}{\lambda_{ij}^a} \right)^{\frac{\lambda_{ij}^a}{\lambda_{ij}^r - \lambda_{ij}^a}}.$$

i and j are the bead types, σ_{ij} indicates the effective bead size and ε_{ij} is the interaction strength between beads i and j . $\lambda_{ij}^a = 6$ and λ_{ij}^r are Mie potential parameters, while r_{ij} is the distance between two CG beads. A universal cutoff for all nonbonded interactions is set to $r_c = 4.583 \sigma$. Units are chosen for the length, σ , energy, ε , mass, m , and time, τ , which in real units would roughly correspond to: $\sigma = 0.43635 \text{ nm}$, $\varepsilon/k_B = 492 \text{ K}$, $m = 44.0521 \text{ amu}$ and $\tau = \sigma(m/\varepsilon)^{0.5} = 1.4062 \text{ ps}$. All simulations are carried out in the NVT ensemble by using the Nosé–Hoover thermostat as implemented in the LAMMPS package^{79,80} with an integration time-step $\delta t = 0.005 \tau$. Moreover, simulations took place at room temperature, therefore, $k_B T/\varepsilon = 0.6057$, which corresponds to $T = 25 \text{ }^\circ\text{C}$.

Surfactants of type C_nEm are considered, such as C10E8 and C10E4. A hydrophobic alkane CG ‘C’ bead represents a $-\text{CH}_2 - \text{CH}_2 - \text{CH}_2 -$ group of atoms, while a hydrophilic CG ‘EO’ bead represents an oxyethylene group $-\text{CH}_2 - \text{O} - \text{CH}_2$. Finally, a water CG ‘W’ bead corresponds to two water molecules. In Table I, the nonbonded interactions between the different CG beads are listed, while the mass of each bead is reported in Table II.

Bonded interactions are taken into account via a harmonic potential, *i.e.*,

$$V(r_{ij}) = 0.5k(r_{ij} - \sigma_{ij})^2 \quad (2)$$

where $k = 295.33 \varepsilon/\sigma^2$. Moreover, EO beads experience a harmonic angle potential:

$$V_\theta(\theta_{ijk}) = 0.5k_\theta(\theta_{ijk} - \theta_0)^2 \quad (3)$$

where θ_{ijk} is the angle between consecutive beads i , j and k . $k_\theta = 4.32 \varepsilon/\text{rad}^2$, while $\theta_0 = 2.75 \text{ rad}$ is the equilibrium angle. Further discussion on the model can be found in previous studies^{62,63}.

To prepare the initial configuration of each system, individual droplets were first equilibrated in the NVT ensemble. The total number of beads in the simulations was 10^5 per initial droplet, with approximately 5% evaporation into the gas. Droplet diameters were $\sim 53 \sigma$, which is about

TABLE I. Mie-potential interaction parameters between CG beads. $\lambda_{ij}^a = 6$ for all cases.

$i-j$	σ_{ij} (σ)	ϵ_{ij} (ϵ/k_B)	λ_{ij}^r
W-W	0.8584	0.8129	8.00
W-C	0.9292	0.5081	10.75
W-EO	0.8946	0.9756	11.94
C-C	1.0000	0.7000	15.00
C-EO	0.9653	0.7154	16.86
EO-EO	0.9307	0.8067	19.00

TABLE II. Mass of CG beads.

Bead type	Mass (m)
W	0.8179
C	0.9552
EO	1.0000

23 nm. Careful consideration was given during the preparation not only to observing the energy of the system, but, also, making sure that the distribution of clusters has reached a dynamic equilibrium and that each cluster was able to diffuse a distance many times its size. After equilibration, the system size (volume of the simulation box) was doubled and droplets were placed next to each other in such a way to avoid interaction between mirror images of the droplets that could potentially occur due to the presence of periodic boundary conditions in all directions, if one was not careful. In this way, the same thermodynamic conditions for the system were approximately guaranteed in the system of a single droplet and in the systems of two droplets used for coalescence. Figure 1a illustrates a typical initial configuration of the system. Only the liquid state (droplets) is shown, which is identified by a cluster analysis^{84,85}, while surrounding vapour has been removed for the sake of clarity. Finally, for our droplets, we have considered a range of different surfactant concentrations below and above the CAC and up to about 6.1 CAC. This covers the whole range of concentrations relevant for the mass transport and other phenomena discussed here.

To quantify the mass transport of surfactant, first a grid with mesh size of 2σ is defined and surfactant and water particles are assigned to each grid cell. The grid size is chosen to guarantee

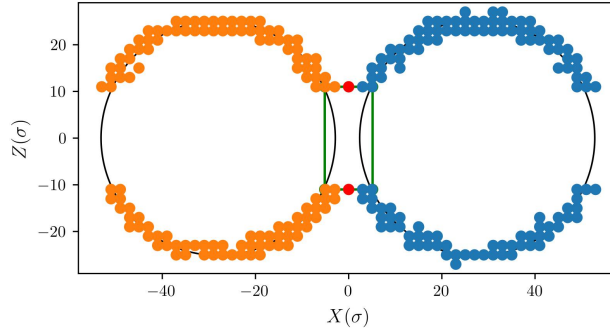


FIG. 2. Specifying the bridge (green rectangle). Orange and blue points are surface grids on left and right droplets, respectively. Red points are the location of highest and lowest beads on bridge. The solid black line is a best fit to the surface grid positions following Ref. 86.

adequate accuracy in the position of the grid cell while avoiding excessive technical randomness due to having a mesh finer than the size of single beads. Then, based on the density, one can identify the grid cells that belong to the droplets surface or the bulk. By following the grid locations of the surfactant beads, we are able to track the transport of surfactant between the different parts of the droplets. The central bead in a molecule determines whether it is counted as bulk or bridge, whereas if any bead of a molecule enters a surface grid cell the molecule is counted as being on the surface.

To track the bridge growth, we need to define the bridge region. In our case, this is a slab whose width in the X direction is recalculated at each snapshot. The left and right limits of the slab are determined by analyzing the grid points on the $X - Z$ plane after droplets have been aligned with the coordinate system as shown in Fig. 2. We fit a circle around each droplet and note the surface grid positions at the central $X = 0$ position, shown by the red points in Fig. 2. Horizontal lines are drawn in the X direction passing through these red points to touch the fitted circles, thus defining the rectangle in green. The vertical sides of the rectangle give the limits of the bridge slab in the X direction and its width. All molecules with centers having X coordinates inside these limits are labelled as belonging to the bridge in a given snapshot.

On the other hand, the bridge radius, b , (Fig. 1) is calculated using the distances between extrema of the positions of the beads belonging to the grids located at $X = 0$, *i.e.* this distance is first calculated separately for the Z coordinate to give a distance $2b_Z$, and then for the Y coordinate to give $2b_Y$. The final bridge radius estimate is then given by $b = (b_Z + b_Y)/2$.

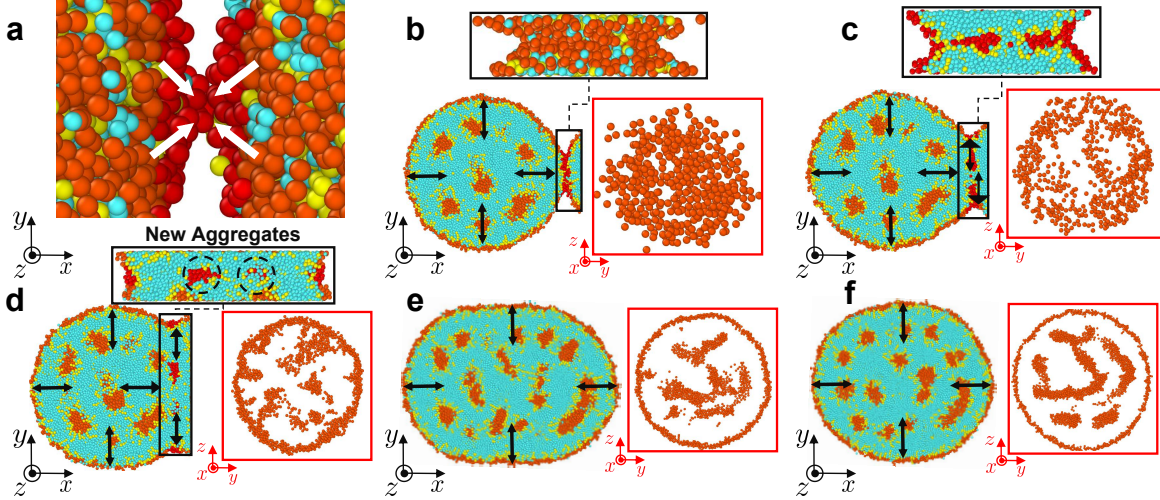


FIG. 3. Mass transport mechanism of surfactant (C10E4 4.7 CAC) during the coalescence process. (a) Droplet pinching (precursor bridge) taking place through the aggregation of surfactant at the first contact point of the droplets ($t - t_c = 6.25 \tau$). Here t_c is the time of first contact; (b) Main surfactant transfer processes during the initial stage of coalescence as indicated by arrows on a droplet cross-section in the $x - y$ plane ($t - t_c = 32.5 \tau$). A larger arrow end indicates the dominant direction of surfactant transport between the different regions in the droplet. Magnified views of the bridge and its cross section on the $y - z$ plane (only hydrophobic beads) are also shown above. At this stage, the bridge is dominated by the presence of surfactant molecules. (c), (d), (e), and (f) at times $t - t_c = 76.25 \tau, t - t_c = 233.75 \tau, t - t_c = 517.50 \tau, t - t_c = 733.75 \tau$, respectively, show evolution in the inertial regime. The snapshots of the system were obtained using Ovito software⁶⁷.

IV. RESULTS AND DISCUSSION

The mass transport mechanism of surfactant molecules during coalescence is fundamental to understanding the role of surfactant in the dynamics of this process at all stages. Surfactant mass transfer mechanisms have been investigated in various processes, for example, superspreading,⁶³ emulsion films,⁴² and foam stabilization in lubricating oils.⁴³ For example, in the case of emulsion films, a fascinating cyclic phenomenon has been observed where new dimples sequentially form with the surfactant redistribution driving this process through coupling to interfacial an hydrodynamic motion inside the films.⁴² In our system, coalescence starts with the formation of the contact point (Fig. 3a), where hydrophobic beads from the two droplets actively move to aggregate due to the favorable attractive interaction. In the case of surfactant-laden droplets, we have

not observed the formation of multiple contact points (bridge precursors) for any of the systems, unlike what has been seen in pure water droplets¹⁰. In fact, water molecules do not participate at this earliest stage in the bridge formation. The bridge growth process continues with the formation of a thin layer of surfactant between the droplets (Fig. 3b), whose origin is mostly from the initial surface coverage. To unveil these processes, we have monitored the transport of surfactant between different parts of the droplets, *i.e.* the interior, the bridge, and their surfaces, which sums up to 36 possible surfactant transport processes. The Supplemental Material (Table S3) provides the numbers for the probabilities of surfactant remaining at a certain place or moving to different parts of the droplets for all cases considered in our study. At this stage, the still small radius, b , of the bridge permits a high supply of surfactant at the contact surface (Fig. 3b), which is central to the coalescence of the droplets. However, as the bridge further grows, the surfactant from the initial contact and inflow to the bridge perimeter is not enough to fully supply the interior of the bridge with surfactant. The perimeter of the bridge grows proportionally to b , while its area (cross-section) increases with b^2 . Therefore, the concentration of surfactant in the bridge, initially very high, reduces proportionally to $1/b$ as the bridge grows. Moreover, tracking the molecules shows that, as the bridge forms, less molecules end up in the bridge bulk than were on the approaching surfaces prior to contact. Surfactant transport towards the surface is favourable energetically and only surfactant that cannot escape to the exterior (surface) remains trapped in the interior of the bridge region. As a result, the engulfed surfactant forms separated aggregates within the bridge, especially for the cases above CAC (Fig. 3d). These aggregates are characteristic of the bridge growth at later stages (Figs 3c–e), and, as we will see later by the analysis of the bridge growth, surfactant from the bulk can join the aggregates that formed at the bridge as it grows.

The relevant surfactant transport processes during the bridge growth that we have identified are the engulfment of surfactant from the contact surface of the droplets into the interior of the bridge (Tables S1 and S2 in the Supplemental Material give details), which increases with surfactant concentration, and to a smaller extent the transfer of surfactant in the bulk towards the bridge (Figs 3c, d). Coalescence is mainly affected by the transfer of surfactant in the region close to the bridge from the interior to the surfaces, while, in the other parts of the droplet, surfactant is rather in dynamic equilibrium and does not affect the coalescence process. After the bridge fully develops (Fig. 3e), a dynamic equilibrium of surfactant extends throughout and no dominant directions of adsorption/desorption processes remain, but only a slight surfactant transport from the surface towards the bulk as the surface area of the droplet becomes smaller. At this final

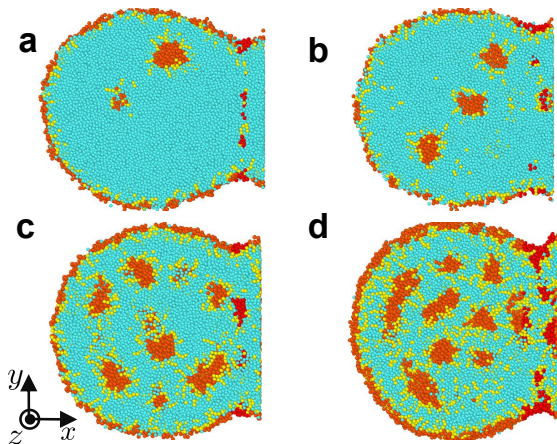


FIG. 4. Droplet interiors in the inertial regime showing the presence of new aggregates emerging during the coalescence process. Cross-sections are shown at times corresponding to Fig. 3d for surfactant in different concentrations of C10E4 above the CAC: (a) 1.6 CAC, (b) 3.2 CAC, (c) 4.7 CAC and (d) 6.1 CAC. The snapshot of the systems were obtained using Ovito software⁶⁷.

stage, the droplet will reach its final spherical shape (Fig. 3f), driven by the surface tension. We have also verified that the new aggregates emerging during the coalescence process consist of surfactant that was previously on the contact area (surfaces) between the two merging droplets. The latter observations are valid throughout a range of different concentrations and surfactants below and above the CAC. Data for other concentrations and surfactants than in Fig. 3 are reported in the Supplemental Material, and show the same mechanism, while snapshots of the aggregate formation in the inertial regime are presented in Fig. 4.

To identify the various regimes and better understand the bridge growth dynamics, we have measured the bridge radius, b , over time for droplets with different surfactant concentrations (Fig. 5 here for C10E4 and Fig. S1 for C10E8 in the Supplemental Material). The regimes that follow after the initial bridge formation can be in principle identified by the bridge radius scaling. The inertial scaling with power law $b \sim \sqrt{t}$ is generally most conspicuous, although we see an apparent changeover from an initial thermal regime (TR) with little bridge growth to the IR power law (see fits in Fig. 5 and Fig. S1 of the Supplemental Material). Moreover, in Fig. 5, the values of the thermal lengths are marked with the horizontal lines for the cases of pure water and surfactant-laden droplets (above CAC) according to previous MD predictions¹⁰. These values are of the same order as the TR regime bridge size that we observe in our data, and express the range of the thermal length scale above which a persistent increase of the bridge radius, b , takes place.

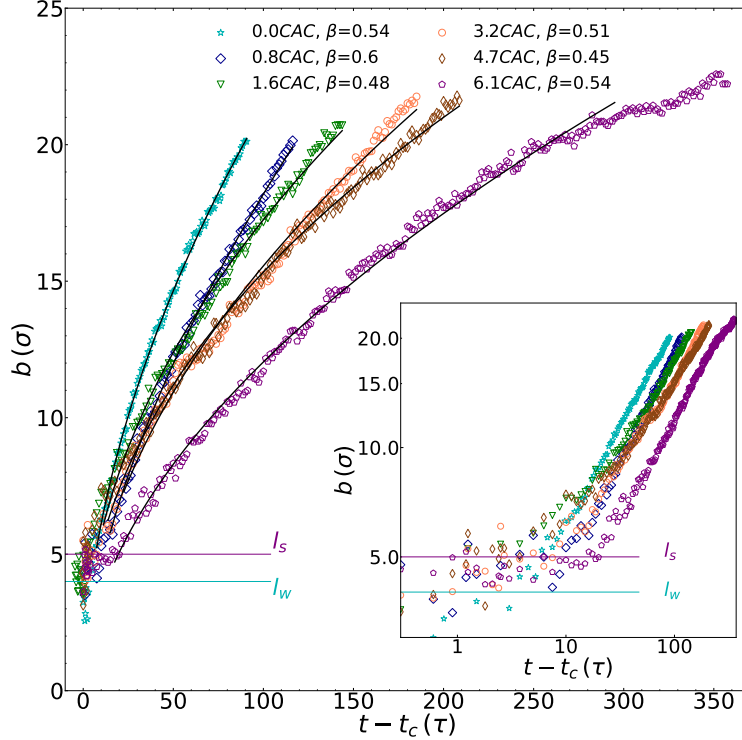


FIG. 5. Bridge growth dynamics (b , radius of the bridge) vs. time, t , for droplets with different surfactant concentrations (C10E4), as indicated in the legend. $CAC \approx 7.5$ wt%. Power law fits are also shown, tentatively identifying the inertial (IR, $b = b_0 t^\beta$) regimes. The inset highlights the power law scaling in the inertial regime and the initial TR regime. l_w is the thermal length for pure water droplets and l_s for surfactant-laden droplets above CAC according to Ref. 10. Data for C10E8 and average growth rates are provided in the Supplemental Material.

Our findings also indicate that the growth speed of the bridge decreases as a function of surfactant concentration in both regimes. Tracking the simulation trajectories we observe that the surfactant aggregates that are present in the bulk can slow the liquid flow and obstruct the strong water–water interactions. Upon a significant increase of surfactant concentration far above CAC, aggregates merge in the bulk leading to an increased rigidity of the droplet. This then hinders the coalescence process by slowing down the rearrangement of the droplet towards its equilibrium spherical shape. This is explained by the interactions of water and hydrophobic beads (see Supplemental Material), which indicate a larger W–W (W: water beads) than C–C (C: hydrophobic surfactant beads) attraction and a strongly unfavorable (less attractive) C–W interaction in comparison to the interactions of all other components. The average bridge growth velocity, which

TABLE III. Average velocity of bridge growth in units σ/τ ^a

Concentration (CAC)	0.8	1.6	3.2	4.7	6.1
C10E4	0.2849	0.2204	0.1878	0.1605	0.1047
C10E8	0.2794	0.2319	0.1871	0.1530	0.1115
CAC = 7.5 wt%					

^a For pure water droplets in the viscous regime (result from simulation): $0.3675 \sigma/\tau$.

includes both the TR and IR regimes together as an overview of the overall speed of growth is reported for each surfactant for a range of concentrations in Table III. It is calculated over the time interval between the moment that the link between the droplets is established, t_c , at the beginning of the coalescence until the point at which the bridge radius is equal to the radius of the droplets in the y direction (for example, see Fig. 3e). As surfactant concentration increases, the bridge growth process slows down in comparison with the simulated case of the pure water droplets. These data also show a slightly faster bridge growth in the case of the C10E8 surfactant (see Fig. S1 in Supplemental Information).

Furthermore, the flow field of water molecules during coalescence exhibits differences between droplets with and without surfactant. In Fig. 6, the colour code indicates flow towards the bridge (red) and away from the bridge (blue). In the case of the water droplets without surfactant, the formation of the bridge at the very initial stages is accompanied by fluctuations of internal collective flow in the direction of the coalescence axis (x direction), which encompass the entire droplets (Figs 6a, b). This is due to the capillary waves produced by the energy release from the initial rupture of the surface when the droplets first touch.⁴⁴ The waves propagate and result in perturbations in the overall shape of the droplets and the flow patterns illustrated in Figs 6a and b. These flow patterns disappear as the bridge grows further and a robust contact between the two droplets establishes beyond the thermal regime. Moreover, an overall flow towards the bridge as the droplets further coalesce is observed (notice the dominance of red in Fig. 6c), while at the final equilibrium only random thermal fluid flow patterns are seen (Fig. 6d). We have not noticed any statistically significant flow patterns or Marangoni flow³³ (*e.g.* in the case of droplets with surfactant) towards any of the other directions (*e.g.* radial).

As surfactant is added to the droplets the early time collective flow patterns of Figs 6a and 6b gradually disappear, especially for all concentrations above the CAC (Fig. 7). Compare, for exam-

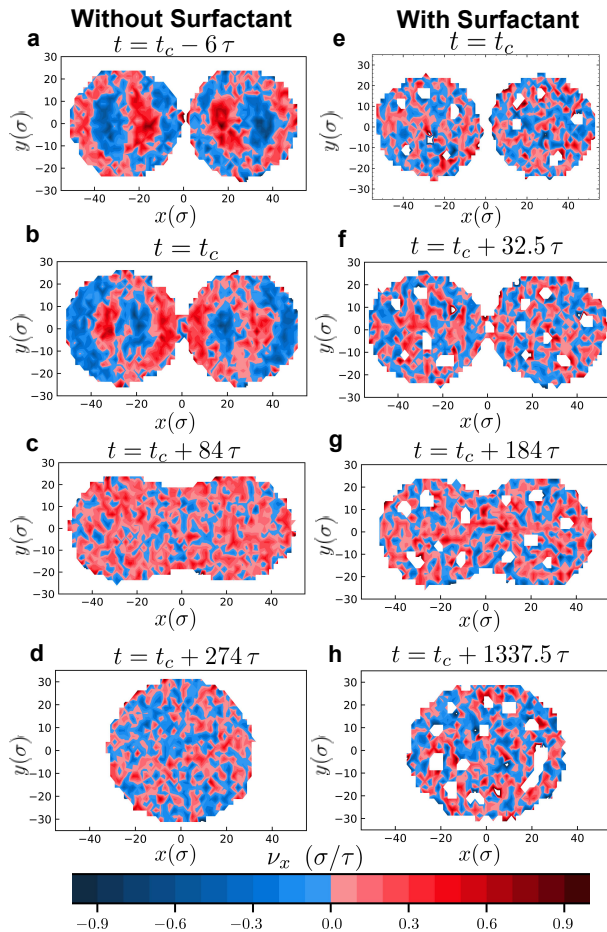


FIG. 6. Flow field of water (x velocity component, v_x), in cross-sections of droplets without (a–d) and with (e–h) surfactant (C10E4) at 4.7 CAC concentration, at different stages of coalescence. Side by side times correspond to similar stages of the coalescence process. Red reflects the intensity of flow (only water) motion towards the bridge, blue away from the bridge. Time labels based on contact time (t_c) are added. Note that white space between the water areas (e.g. in the bridge) includes surfactant aggregates and surfactant on the surface. This can cause an illusion of multiple contact points such as in panel f, which are in fact surrounded by surfactant forming an overall broad bridge.

ple, the flow patterns in Fig. 6b and 6f, for the same bridge size. The suppression of the collective flow occurs through two routes: First, the surfactant at the surface reduces the surface tension (reducing energy input from the initial rupture of the surface) and, also, reduces the amplitude of thermal fluctuations, thus suppressing the formation of multiple thermal bridges¹⁰. Second, the presence of aggregates in the bulk hinders the flow of the water molecules and disperses the momentum transfer before it enters deeper into the droplets.

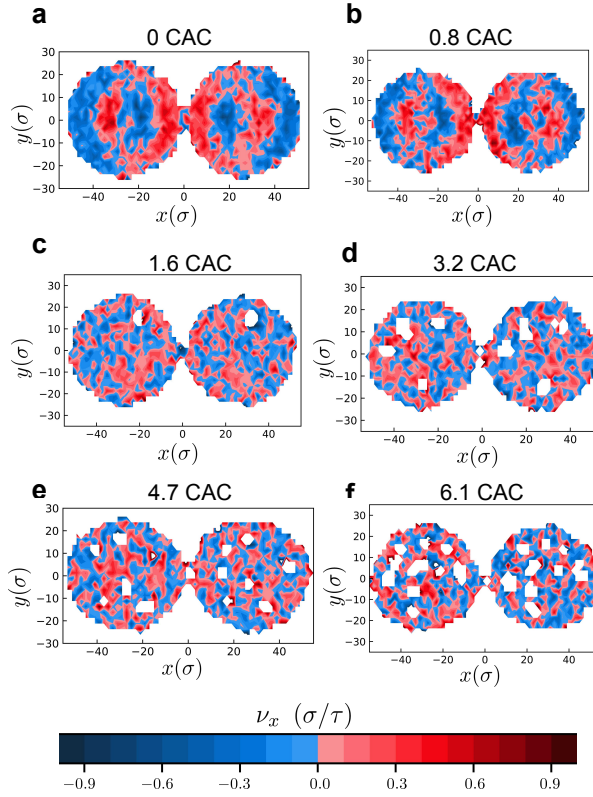


FIG. 7. Water flow pattern for different concentrations (a–f, 0–6.1 CAC) for C10E4 at the initial pinching stage. Above CAC (c–f), there is no observable pattern. Red color reflects the intensity of flow towards the bridge, while blue indicates the intensity of flow away from the bridge. Like in Fig. 6, empty space within/between the water in the droplets (e.g. in the bridge) includes surfactant, and the contact point of the droplet surface is always single.

V. CONCLUSIONS

In this study, the fundamental processes involved in coalescence of droplets containing surfactant have been described — including the initial rupture and bridge growth, which occur on time and length scales inaccessible to experiment. We have reported on the main adsorption processes (surfactant transport mechanism), characterised the bridge growth dynamics of coalescence, and identified several important differences to the case of pure water droplets and those with surfactant. Notably, Fig. 5 suggests that if a slow-down of coalescence processes is desired industrially, more surfactant should be added, which confirms earlier suggestions^{37,57}. Moreover, we have identified early time collective flow patterns that are present in the case of aqueous droplets without surfactant, but are absent when appreciable surfactant is present. Surfactant also suppresses the multiple

precursor bridges that are important at early times for pure water¹⁰. The last appears to indicate that thermal fluctuations will be less important for topological changes of surfactant-laden droplets generally (splitting, merging, etc.). We anticipate that our results open new exploration directions, which will be relevant for practical applications, and that they suggest the kind of effects that will be seen in other as yet unexplored processes such as droplet break-up and coalescence on substrates. An aspect that requires further consideration is the various effects that might be attributed to a larger surface-area-to-volume ratio as the size of the droplets decreases. For example, we saw that minor redistribution of surfactants from surface to bulk or vice versa can cause large fluctuations in the bulk, while such effects may become negligible in macroscale systems.²⁶ It would therefore be interesting to explore larger systems in the future as more computational resources become available, as well as employ a range of different simulation models to explore droplet coalescence in the presence of surfactant.

VI. SUPPLEMENTARY MATERIAL

The Supplementary Material provides the details of the probabilities for the mass transport mechanism of surfactant molecules between the different regions in the droplets that reflect the arrows in Fig. 3. It also contains data on the bridge growth dynamics in the case of C10E8 surfactant.

ACKNOWLEDGMENTS

This research has been supported by the National Science Centre, Poland, under grant No. 2019/34/E/ST3/00232. We gratefully acknowledge Polish high-performance computing infrastructure PLGrid (HPC Centers: ACK Cyfronet AGH) for providing computer facilities and support within computational grant no. PLG/2022/015261.

REFERENCES

- ¹E. G. Bowen, “The formation of rain by coalescence,” *Aust. J. Sci. Res., Ser. A; Phys. Sci.* **3**, 193–214 (1950).
- ²E. X. Berry and R. L. Reinhardt, “An analysis of cloud drop growth by collection: part 3. accretion and self-collection,” *J. Atmos. Sci.* **31**, 2118–2126 (1974).

- ³D. Campana, J. D. Paolo, and F. A. Saita, “A 2-d model of rayleigh instability in capillary tubes — surfactant effects,” *Int. J. Multiphase Flow* **50**, 431–454 (2004).
- ⁴J. Lu and C. M. Corvalan, “Coalescence of viscous drops with surfactants,” *Chem. Eng. Sci.* **78**, 9–13 (2012).
- ⁵M. Singh, H. Haverinen, P. Dhagat, and G. Jabbour, “Inkjet printing process and its applications,” *Adv. Mater.* **22**, 673–685 (2010).
- ⁶A. Frohn and N. Roth, *Dynamics of Droplets* (Springer, Berlin, 2000).
- ⁷J. D. Paulsen, R. Carmigniani, A. Kannan, J. C. Burton, and S. R. Nagel, “Coalescence of bubbles and drops in an outer fluid,” *Nat. Commun.* **5**, 3182 (2014).
- ⁸Y. Yoon, F. Baldessari, H. D. Ceniceros, and L. G. Leal, “Coalescence of two equal-sized deformable drops in an axisymmetric flow,” *Phys. Fluids* **19**, 102102 (2007).
- ⁹M. I. Khodabocus, M. Sellier, and V. Nock, “Scaling laws of droplet coalescence: Theory and numerical simulation,” *Adv. Math. Phys.* **2018** (2018).
- ¹⁰S. Perumanath, M. K. Borg, M. V. Chubynsky, J. E. Sprittles, and J. M. Reese, “Droplet coalescence is initiated by thermal motion,” *Phys. Rev. Lett.* **122**, 104501 (2019).
- ¹¹J. Eggers, J. R. Lister, and H. A. Stone, “Coalescence of liquid drops,” *J. Fluid Mech.* **401**, 293–310 (1999).
- ¹²D. G. Aarts, H. N. Lekkerkerker, H. Guo, G. H. Wegdam, and D. Bonn, “Hydrodynamics of droplet coalescence,” *Phys. Rev. Lett.* **95**, 164503 (2005).
- ¹³J. E. Sprittles and Shikhmurzaev, “Coalescence of liquid drops: Different models versus experiment,” *Phys. Fluids* **24**, 122105 (2012).
- ¹⁴M. Dudek, D. Fernandes, E. Helno Herø, and G. Øye, “Microfluidic method for determining drop-drop coalescence and contact times in flow,” *Colloids Surf. A: Physicochem. Eng. Asp.* **586**, 124265 (2020).
- ¹⁵M. M. Rahman, W. Lee, A. Iyer, and S. J. Williams, “Viscous resistance in drop coalescence,” *Phys. Fluids* **31**, 012104 (2019).
- ¹⁶J. D. Berry and R. R. Dagastine, “Mapping coalescence of micron-sized drops and bubbles,” *J. Colloid Interface Sci.* **487**, 513–522 (2017).
- ¹⁷P. M. Somwanshi, K. Muralidhar, and S. Khandekar, “Coalescence dynamics of sessile and pendant liquid drops placed on a hydrophobic surface,” *Phys. Fluids* **30**, 092103 (2018).
- ¹⁸P. K. Kirar, K. Alvarenga, P. Kolhe, G. Biswas, and K. Chandra Sahu, “Coalescence of drops on the free-surface of a liquid pool at elevated temperatures,” *Phys. Fluids* **32**, 052103 (2020).

- ¹⁹S. Bayani, Y. Tabe, Y. T. Kang, S. H. Lee, and C. K. Choi, “Surface plasmon resonance imaging of drop coalescence at high-temporal resolution,” *J. Flow Vis. Image Process.* **25**, 191–205 (2018).
- ²⁰M. Brik, S. Harmand, and I. Zaaroura, “Relaxation and contact angle dynamics during the coalescence of different sized vertically aligned water drops in different silicone oil viscosities,” *Colloids Surf. A: Physicochem. Eng. Asp.* **629**, 127429 (2021).
- ²¹C. R. Anthony, M. T. Harris, and O. A. Basaran, “Initial regime of drop coalescence,” *Phys. Rev. Fluids* **5**, 033608 (2020).
- ²²V. R. Kern, T. Sæter, and A. Carlson, “Viscoplastic sessile drop coalescence,” *Phys. Rev. Fluids* **7**, L081601 (2022).
- ²³M. Heinen, M. Hoffmann, F. Diewald, S. Seckler, K. Langenbach, and J. Vrabec, “Droplet coalescence by molecular dynamics and phase-field modeling,” *Phys. Fluids* **34**, 042006 (2022).
- ²⁴M. Geri, B. Keshavarz, G. H. McKinley, and J. W. M. Bush, “Thermal delay of drop coalescence,” *J. Fluid Mech.* **833**, R3 (2017).
- ²⁵M. Abouelsoud and B. Bai, “Bouncing and coalescence dynamics during the impact of a falling drop with a sessile drop on different solid surfaces,” *Phys. Fluids* **33**, 063309 (2021).
- ²⁶N. I. Politova, S. Tcholakova, S. Tsibranska, N. D. Denkov, and K. Muelheims, “Coalescence stability of water-in-oil drops: Effects of drop size and surfactant concentration,” *Colloids Surf. A: Physicochem. Eng. Asp.* **531**, 32–39 (2017).
- ²⁷W. H. Weheliye, T. Dong, and P. Angeli, “On the effect of surfactants on drop coalescence at liquid/liquid interfaces,” *Chem. Eng. Sci.* **161**, 215–227 (2017).
- ²⁸G. Soligo, A. Roccon, and A. Soldati, “Coalescence of surfactant-laden drops by phase field method,” *J. Comput. Phys.* **376**, 1292–1311 (2019).
- ²⁹T. Dong, W. H. Weheliye, P. Chausset, and P. Angeli, “An experimental study on the drop/interface partial coalescence with surfactants,” *Phys. Fluids* **29**, 102101 (2017).
- ³⁰T. Dong, W. H. Weheliye, and P. Angeli, “Laser induced fluorescence studies on the distribution of surfactants during drop/interface coalescence,” *Phys. Fluids* **31**, 012106 (2019).
- ³¹N. M. Kovalchuk, M. Reichow, T. Frommweiler, D. Vigolo, and M. J. H. Simmons, “Mass transfer accompanying coalescence of surfactant-laden and surfactant-free drop in a microfluidic channel,” *Langmuir* **35**, 9184–9193 (2019).
- ³²T. C. Botti, A. Hutin, E. Quintella, and M. S. Carvalho, “Effect of interfacial rheology on drop coalescence in water–oil emulsion,” *Soft Matter* **18**, 1423–1434 (2022).

- ³³C. Constante-Amores, A. Batchvarov, L. Kahouadji, S. Shin, J. Chergui, D. Juric, and O. Matar, “Role of surfactant-induced marangoni stresses in drop-interface coalescence,” *J. Fluid Mech.* **925**, A15 (2021).
- ³⁴M. Kasmaee, F. Varaminian, P. Khadiv-Parsi, and J. Saien, “Effects of different surfactants and physical properties on the coalescence of dimethyl disulfide drops with mother phase at the interface of sodium hydroxide aqueous solutions,” *J. Mol. Liq.* **263**, 31–39 (2018).
- ³⁵E. Nowak, Z. Xie, N. M. Kovalchuk, O. K. Matar, and M. J. Simmons, “Bulk advection and interfacial flows in the binary coalescence of surfactant-laden and surfactant-free drops,” *Soft Matter* **13**, 4616–4628 (2017).
- ³⁶E. Nowak, N. M. Kovalchuk, Z. Che, and M. J. Simmons, “Effect of surfactant concentration and viscosity of outer phase during the coalescence of a surfactant-laden drop with a surfactant-free drop,” *Colloids Surf. A Physicochem. Eng. Asp.* **505**, 124–131 (2016).
- ³⁷N. Jaensson and J. Vermant, “Tensiometry and rheology of complex interfaces,” *Curr. Opin. Colloid Interface Sci.* **37**, 136–150 (2018).
- ³⁸S. Narayan, A. E. Metaxa, R. Bachnak, T. Neumiller, C. S. Dutcher, *et al.*, “Zooming in on the role of surfactants in droplet coalescence at the macro-and microscale,” *Curr. Opin. Colloid Interface Sci.* (2020).
- ³⁹I. B. Ivanov, K. D. Danov, and P. A. Kralchevsky, “Flocculation and coalescence of micron-size emulsion droplets,” *Colloids Surf. A Physicochem. Eng.* **152**, 161–182 (1999).
- ⁴⁰S. Tcholakova, N. D. Denkov, and T. Danner, “Role of surfactant type and concentration for the mean drop size during emulsification in turbulent flow,” *Langmuir* **20**, 7444–7458 (2004).
- ⁴¹D. Langevin, “Coalescence in foams and emulsions: Similarities and differences,” *Curr. Opin. Colloid Interface Sci.* **44**, 23–31 (2019).
- ⁴²O. D. Velev, T. D. Gurkov, and R. P. Borwankar, “Spontaneous cyclic dimpling in emulsion films due to surfactant mass transfer between the phases,” *J. Colloid Interface Sci.* **159**, 497–501 (1993).
- ⁴³V. C. Suja, A. Kar, W. Cates, S. M. Remmert, P. D. Savage, and G. G. Fuller, “Evaporation-induced foam stabilization in lubricating oils,” *Proc. Natl. Acad. Sci. U.S.A.* **115**, 7919–7924 (2018).
- ⁴⁴P. J. Dekker, M. A. Hack, W. Tewes, C. Datt, A. Bouillant, and J. H. Snoeijer, “When elasticity affects drop coalescence,” *Phys. Rev. Lett.* **128**, 028004 (2022).

- ⁴⁵E. Calvo, E. de Malmazet, F. Risso, and O. Masbernat, “Coalescence of water drops at an oil–water interface loaded with microparticles and surfactants,” *Ind. Eng. Chem. Res.* **58**, 15573–15587 (2019).
- ⁴⁶S. Arbabi and P. E. Theodorakis, “Coalescence of sessile polymer droplets: A molecular dynamics study,” *Macromol. Theory Simul.* **n/a**, 2300017 (2023).
- ⁴⁷S. C. Varma, A. Saha, and A. Kumar, “Coalescence of polymeric sessile drops on a partially wettable substrate,” *Phys. Fluids* **33**, 123101 (2021).
- ⁴⁸V. S. Sivasankar, S. A. Etha, D. R. Hines, and S. Das, “Coalescence of microscopic polymeric drops: Effect of drop impact velocities,” *Langmuir* **37**, 13512–13526 (2021).
- ⁴⁹V. S. Sivasankar, D. R. Hines, and S. Das, “Numerical study of the coalescence and mixing of drops of different polymeric materials,” *Langmuir* **38**, 14084–14096 (2022).
- ⁵⁰M. R. Otazo, R. Ward, G. Gillies, R. S. Osborne, M. Golding, and M. A. K. Williams, “Aggregation and coalescence of partially crystalline emulsion drops investigated using optical tweezers,” *Soft Matter* **15**, 6383–6391 (2019).
- ⁵¹C. Vannozzi, “Effect of polymer-coated gold nanoparticle stabilizers on drop coalescence,” *Phys. Fluids* **31**, 082112 (2019).
- ⁵²A. Kovetz and B. Olund, “The effect of coalescence and condensation on rain formation in a cloud of finite vertical extent,” *J. Atmos. Sci.* **26**, 1060–1065 (1969).
- ⁵³S. Feng, L. Yi, L. Zhao-Miao, C. Ren-Tuo, and W. Gui-Ren, “Advances in micro-droplets coalescence using microfluidics,” *Chinese J. Anal. Chem.* **43**, 1942–1954 (2015).
- ⁵⁴W. Ristenpart, P. McCalla, R. Roy, and H. Stone, “Coalescence of spreading droplets on a wettable substrate,” *Phys. Rev. Lett.* **97**, 064501 (2006).
- ⁵⁵M. Dudek, J. Chicault, and G. Øye, “Microfluidic investigation of crude oil droplet coalescence: effect of oil/water composition and droplet aging,” *Energy Fuels* **34**, 5110–5120 (2019).
- ⁵⁶L. Duchemin, J. Eggers, and C. Josserand, “Inviscid coalescence of drops,” *J. Fluid Mech.* **487**, 167–178 (2003).
- ⁵⁷L. Leal, “Flow induced coalescence of drops in a viscous fluid,” *Phys. Fluids* **16**, 1833–1851 (2004).
- ⁵⁸M. Chinaud, V. Voulgaropoulos, and P. Angeli, “Surfactant effects on the coalescence of a drop in a hele-shaw cell,” *Phys. Rev. E* **94**, 033101 (2016).

- ⁵⁹L. Y. Yeo, O. K. Matar, E. S. P. de Ortiz, and G. F. Hewitt, “Film drainage between two surfactant-coated drops colliding at constant approach velocity,” *J. Colloid Interface Sci.* **257**, 93–107 (2003).
- ⁶⁰Y. Hu, D. Pine, and L. G. Leal, “Drop deformation, breakup, and coalescence with compatibilizer,” *Phys. Fluids* **12**, 484–489 (2000).
- ⁶¹A. Mansouri, H. Arabnejad, and R. Mohan, “Numerical investigation of droplet-droplet coalescence and droplet-interface coalescence,” in *Fluids Engineering Division Summer Meeting*, Vol. 46216 (American Society of Mechanical Engineers, 2014) p. V01AT05A006.
- ⁶²P. E. Theodorakis, E. A. Müller, R. V. Craster, and O. K. Matar, “Modelling the superspreading of surfactant-laden droplets with computer simulation,” *Soft Matter* **11**, 9254–9261 (2015).
- ⁶³P. E. Theodorakis, E. A. Müller, R. V. Craster, and O. K. Matar, “Superspreading: Mechanisms and molecular design,” *Langmuir* **31**, 2304–2309 (2015).
- ⁶⁴P. E. Theodorakis, E. R. Smith, R. V. Craster, E. A. Müller, and O. K. Matar, “Molecular dynamics simulation of the superspreading of surfactant-laden droplets. a review,” *Fluids* **4**, 176 (2019).
- ⁶⁵P. E. Theodorakis, E. A. Müller, R. V. Craster, and O. K. Matar, “Insights into surfactant-assisted superspreading,” *Curr. Opin. Colloid Interface Sci.* **19**, 283–289 (2014).
- ⁶⁶P. E. Theodorakis, E. R. Smith, and Müller, “Spreading of aqueous droplets with common and superspreading surfactants. a molecular dynamics study,” *Coll. Surf. A: Physicochem. Eng. Asp.* **581**, 123810 (2019).
- ⁶⁷A. Stukowski, “Visualization and analysis of atomistic simulation data with ovito—the open visualization tool,” *Modelling Simul. Mater. Sci. Eng.* **18**, 015012 (2010).
- ⁶⁸J. Jin, C. H. Ooi, D. V. Dao, and N.-T. Nguyen, “Coalescence processes of droplets and liquid marbles,” *Micromachines* **8**, 336 (2017).
- ⁶⁹J. D. Paulsen, J. C. Burton, S. R. Nagel, S. Appathurai, M. T. Harris, and O. A. Basaran, “The inexorable resistance of inertia determines the initial regime of drop coalescence,” *Proc. Natl. Acad. Sci. U.S.A.* **109**, 6857–6861 (2012).
- ⁷⁰J. D. Paulsen, “Approach and coalescence of liquid drops in air,” *Phys. Rev. E* **88**, 063010 (2013).
- ⁷¹H. Xu, T. Wang, and Z. Che, “Bridge evolution during the coalescence of immiscible droplets,” *J. Colloid Interface Sci.* **628**, 869–877 (2022).
- ⁷²J. D. Paulsen, J. C. Burton, and S. R. Nagel, “Viscous to inertial crossover in liquid drop coalescence,” *Phys. Rev. Lett.* **106**, 114501 (2011).

- ⁷³F. Jin, R. Balasubramaniam, and K. J. Stebe, “Surfactant adsorption to spherical particles: The intrinsic length scale governing the shift from diffusion to kinetic-controlled mass transfer,” *J. Adhes.* **80**, 773–796 (2004).
- ⁷⁴E. A. Müller and G. Jackson, “Force field parameters from the SAFT- γ equation of state for use in coarse-grained molecular simulations,” *Annu. Rev. Chem. Biomol. Eng.* **5**, 405–427 (2014).
- ⁷⁵O. Lobanova, C. Avendaño, T. Lafitte, E. A. Müller, and G. Jackson, “SAFT- γ force field for the simulation of molecular fluids. 4. a single-site coarse-grained model of water applicable over a wide temperature range.” *Mol. Phys.* **113**, 1228–1249 (2015).
- ⁷⁶T. Lafitte, A. Apostolakou, C. Avendaño, A. Galindo, C. S. Adjiman, E. A. Müller, and G. Jackson, “Accurate statistical associating fluid theory for chain molecules formed from mie segments,” *J. Chem. Phys.* **139**, 154504 (2013).
- ⁷⁷C. Avendaño, T. Lafitte, A. Galindo, C. S. Adjiman, G. Jackson, and E. A. Müller, “Saft- γ force field for the simulation of molecular fluids. 1. a single-site coarse grained model of carbon dioxide,” *J. Phys. Chem B* **115**, 11154–11169 (2011).
- ⁷⁸C. Avendaño, T. Lafitte, A. Galindo, C. S. Adjiman, E. A. Müller, and G. Jackson, “Saft- γ force field for the simulation of molecular fluids: 2. coarse-grained models of greenhouse gases,” *J. Phys. Chem B* **117**, 2717–2733 (2013).
- ⁷⁹S. Plimpton, “Fast parallel algorithms for short-range molecular dynamics,” *J. Comp. Phys.* **117**, 1–19 (1995).
- ⁸⁰A. P. Thompson, H. M. Aktulga, R. Berger, D. S. Bolintineanu, W. M. Brown, P. S. Crozier, P. J. in ’t Veld, A. Kohlmeyer, S. G. Moore, T. D. Nguyen, R. Shan, M. J. Stevens, J. Tranchida, C. Trott, and S. J. Plimpton, “LAMMPS - a flexible simulation tool for particle-based materials modeling at the atomic, meso, and continuum scales,” *Comp. Phys. Comm.* **271**, 108171 (2022).
- ⁸¹O. Lobanova, *Development of coarse-grained force fields from a molecular based equation of state for thermodynamic and structural properties of complex fluids*, Ph.D. thesis, Imperial College London (2014).
- ⁸²O. Lobanova, A. Mejia, G. Jackson, and E. A. Müller, “Saft- γ force field for the simulation of molecular fluids 6: Binary and ternary mixtures comprising water, carbon dioxide, and n-alkanes,” *J. Chem. Thermodyn.* **93**, 320–336 (2016).
- ⁸³P. Morgado, O. Lobanova, E. A. Müller, G. Jackson, M. Almeida, and E. J. Filipe, “Saft- γ force field for the simulation of molecular fluids: 8. hetero-segmented coarse-grained models

- of perfluoroalkylalkanes assessed with new vapour–liquid interfacial tension data,” *Mol. Phys.* **114**, 2597–2614 (2016).
- ⁸⁴P. E. Theodorakis, W. Paul, and K. Binder, “Pearl-necklace structures of molecular brushes with rigid backbone under poor solvent conditions: A simulation study,” *J. Chem. Phys.* **133**, 104901 (2010).
- ⁸⁵P. E. Theodorakis, W. Paul, and K. Binder, “Analysis of the cluster formation in two-component cylindrical bottle-brush polymers under poor solvent conditions. a simulation study,” *Eur. Phys. J. E* **34**, 52 (2011).
- ⁸⁶K. Kanatani and P. Rangarajan, “Hyper least squares fitting of circles and ellipses,” *Comput. Stat. Data Anal.* **55**, 2197–2208 (2011).